Inorganic Chemistry

pubs.acs.org/IC Article

Magnetic Kagome Lattice (Gd,Tb,Dy,Ho,Er)Mn_6Sn_6 with High Configuration Entropy

Published as part of Inorganic Chemistry special issue "Quantum Materials from an Inorganic Chemistry Perspective".

Wenhao Liu, Nikhil Uday Dhale, Youzhe Chen, Pramanand Joshi, Zixin Zhai, Xiqu Wang, J. Ping Liu, Robert J. Birgeneau, Boris Maiorov, Christopher A. Mizzi, and Bing Lv*

Cite This: *Inorg. Chem.* 2026, 65, 71−78 Read Online

ACCESS | Metrics & More | Article Recommendations | Supporting Information

ABSTRACT: The magnetic kagome lattice compound RMn_6Sn_6 (R = rare earth) is an emerging platform to exploit the interplay between magnetism and topological electronic states, where a variety of exciting findings, such as flat bands and Dirac points, as well as the dramatic dependence of magnetic order on the rare-earth element, have been reported. High configurational entropy through rare earth alloying, on the other hand, provides another knob to control the physical properties in this system. Here, by the marriage of high entropy and the magnetic Kagome lattice, we obtain (Gd,Tb,Dy,Ho,Er)Mn_6Sn_6 single crystals and systematically investigate their magnetic and transport properties. Different from the parent phases, the high entropy 166 material displays multiple novel magnetic transitions induced by temperature and external magnetic fields. Furthermore, linear magnetoresistance persisting up to 20 T has been revealed at 4 K. The intrinsic nontrivial band topology also survives in the high-entropy phase, as evidenced by the intrinsic anomalous Hall effect. Our study offers a glimpse into a vast compositional landscape that holds high promises for uncovering new magnetic and topological phenomena.

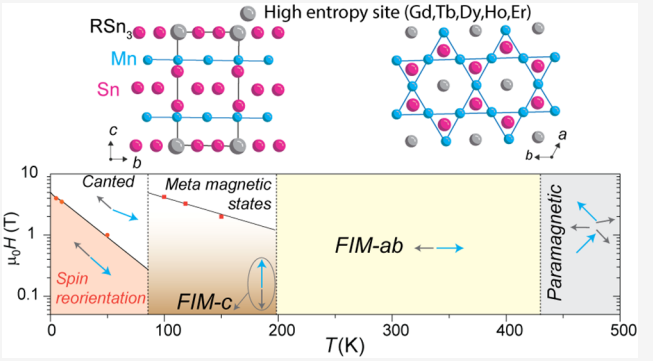

1. INTRODUCTION

The kagome lattice has received great attention recently due to the novel physics and the associated interesting properties arising from the interplay between electron correlations and lattice geometry. A typical kagome lattice consists of corner-shared triangles, forming a distinctive honeycomb-like structure.[1] This unique geometry has great potential to realize novel band structures, including flat bands, linear band crossings forming Dirac/Weyl points, and van Hove singularities, which harbor important correlated electronic states and lead to rich interesting phenomena such as unconventional superconductivity,[2] dissipationless spin moment locked charge transport, and large quantum anomalous Hall effects.[3,4] Introducing magnetic ions into a geometrically frustrated Kagome lattice provides another tool to tune these correlated electronic states. A prime example is hexagonal RMn_6Sn_6 (R166), where R represents transition metal elements like Sc, Y, and rare-earth elements La−Lu. These compounds usually consist of two sublattices: a Mn−Sn layer with a Kagome lattice of Mn and a triangular R-Sn layer. The Mn kagome layer shows strong ferromagnetic in-plane coupling,[5] which results in magnetic order above room temperature. On the other hand, Mn and the rare-earth elements are generally antiferromagnetically coupled.[6,7] Competition between these ferromagnetic and antiferromagnetic couplings results in rich magnetic phases. For example, collinear ferrimagnetic order (FIM) in (Gd−Ho)Mn_6Sn_6 emerges when strong antiferromagnetic coupling between the Gd−Ho and Mn sublattices dominates. For nonmagnetic elements Sc and Y, the ferromagnetic coupling between Mn is the strongest and their R166 phases show a spiral magnetic structure in which the ferromagnetic magnetic order rotates among adjacent Mn layers.[7−9] The coupling between Mn and Er is at the boundary between the formation of FIM in (Gd−Ho)Mn_6Sn_6 and the spiral magnetism in (Y, Sc)Mn_6Sn_6. As a result, $ErMn_6Sn_6$ shows an interesting triple-spiral magnetic ordering[10,11] and topological Hall effect.[7,9,12] As a whole, R166 shows unique temperature and field-driven magnetic insta-

Received: July 26, 2025
Revised: December 1, 2025
Accepted: December 22, 2025
Published: December 28, 2025

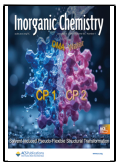

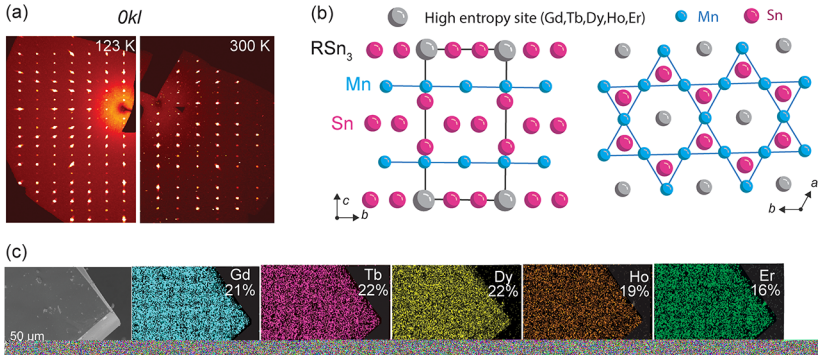

Figure 1. Structure and composition of HE166. (a) Precession image of HE166 obtained from an X-ray diffractometer at room temperature at 300 K and low temperature at 123 K. (b) Crystal structure of HE166 viewed along the crystallographic *a* and *c* axes. (c) SEM-EDX mapping revealed the chemical distribution of the rare-earth elements in HE166, highlighting the homogeneous distribution of the five rare-earth elements.

bilities, opening new avenues in topological and magnetic state control and switching.[13]

High entropy is another concept that has received great attention in the past decade. It is an alloying strategy that yields a single-phase random distribution of solid solution with five or more elements.[1,14,15] The formation of high-entropy materials relies on the configuration entropy contributing to the free energy sufficiently to overcome the formation enthalpy, resulting in a highly disordered, yet chemically homogeneous system. This high degree of homogeneity in high-entropy materials plays a crucial role in including various material properties like mechanical, electronic and magnetic characteristics.[15−18] Moreover, it provides a vast compositional space with diverse combinations of composition, charge, and spin, enabling the exploration of a much wider range of novel correlated phenomena.[1,14] Motivated by the potential advantages of this strategy and the rich magnetic structures specified by individual rare-earth elements in the R166 system, we synthesized and characterized a new high-entropy kagome lattice by incorporating five rare-earth elements, Gd, Tb, Dy, Ho, and Er, on the same crystallographic site, forming a high-entropy kagome phase in $(Gd_{0.21}Tb_{0.22}Dy_{0.22}Ho_{0.19}Er_{0.16})Mn_6Sn_6$, denoted as HE166 in the main text. Large-sized single crystals have been successfully grown via Sn flux method. A cascade of new phenomena emerges in this high-entropy kagome system that is not found in the parent compounds. Magnetic measurements reveal multiple magnetic transitions including ferrimagnetic transitions and spin reorientations. The application of an external magnetic field additionally induces multiple field-dependent transitions including metamagnetic states and possibly chiral magnetic order. Correlated with magnetization, our electrical transport results show a first-order phase transition around 205 K. Magneto-transport measurements exhibit a linear, nonsaturating magnetoresistance persisting up to 20 T, potentially linked to the band topology and the high-entropy effects. Hall measurements further reveal the intrinsic Hall effect and nonzero internal Hall conductivity, indicating the survival of Chern gapped Dirac Fermions that exist in the parent phases. During the progress of our research work, we also became aware of a prior study that successfully synthesized a four-rare-earth high-entropy Kagome alloy, $(Gd,Tb,Dy,Ho)Mn_6Sn_6$.[19] Their four-component high-entropy phase exhibits magnetic behaviors distinct from those observed in our five rare-earth high-entropy phases reported here, and both differ significantly from those of the single rare-earth RMn_6Sn_6 compounds.

2. MATERIALS AND METHODS

2.1. Material Synthesis. High entropy 166 single crystals were synthesized using a flux method, where Sn is used as the flux. High-purity Gd (Alfa Aesar, 99%), Tb (Alfa Aesar, 99.9%), Dy (Alfa Aesar, 99.8%), Ho (Alfa Aesar, 99.9%), and Er (Alfa Aesar, 99.9%) were filed from ingots and then mixed with Mn (Alfa Alser, 99.99%) pieces and Sn (Alfa Aesar 99.9999%) ingots with a ratio of 0.2:0.2:0.2:0.2:0.2:6:20. The mixtures were placed in an alumina crucible and subsequently sealed in an evacuated quartz tube. The assembly was heated up to 1100 °C in a furnace and held at this temperature for 2 days, which is followed by cooling to 600 °C at a rate of 1 °C/h. After the tube was centrifuged at 600 °C, large-size single crystals with an average lateral size of 5 × 5 mm^2 were obtained.

The chemical composition of the yield crystals was verified by energy-dispersive X-ray spectroscopy (EDX) on a DM07 Zeiss Supra 40 scanning electron microscope. The crystal structure of the HE166 phase was determined by single-crystal X-ray data measured on a Bruker DUO diffractometer equipped with an Apex-II area detector and an Oxford Cryosystems 700 Series temperature controller with a Mo *Kα* source (λ = 0.7103Å). The collected data set was integrated using the Bruker Apex-II program, with the intensities corrected for the Lorentz factor, polarization, air absorption, and absorption due to variation in the path length through the detector faceplate. The data were scaled, and absorption correction was applied using SADABS. The structure was solved using the intrinsic phasing method in SHELXT and refined using SHELXL with all atoms refined anisotropically.

2.2. Magnetization and Transport Measurement. DC magnetization measurement was conducted with a Quantum Design Magnetic Property Measurement System (MPMS3) down to 5 K. Resistivity and Hall signals of HE166 single crystals were measured using a Quantum Design Physical Property Measurement System (PPMS) with the temperature range of 5 to 300 K and the magnetic fields up to 9 T. Measurements in pulsed magnets were conducted at the National High Magnetic Field Laboratory's Pulsed Field Facility in Los Alamos National Laboratory. Four-wire electrical resistance measurements were performed in a 65T short-pulse magnet with a He-4 cryostat. Owing to the small resistance of the sample, resistance was measured with a pulsed direct current method based upon a modified form of the approach described in ref.[20] Typical current durations were ∼10 μs. Each data set is the average of multiple pulses to improve the signal-to-noise ratio, and the resistances were symmetrized with respect to the direction of the applied magnetic field. The maximum applied magnetic field was limited by the strong torque response of the sample.

3. RESULTS AND DISCUSSION

The crystal structure of HE166 with five rare-earth elements was determined by using an X-ray diffractometer on the single crystals. Figure 1a presents the procession image of (*0kl*) zone,

https://doi.org/10.1021/acs.inorgchem.5c03461
Inorg. Chem. 2026, 65, 71−78

Table 1. Crystallographic Data of $HEMn_6Sn_6$ at 123 and 300 K

Compounds	$(Gd_{0.21},Tb_{0.22},Dy_{0.22},Ho_{0.19},Er_{0.16})Mn_6Sn_6$	
Temperature	123 K	300 K
Crystal symmetry	hexagonal	hexagonal
Space Group	*P6/mmm* (No.191)	*P6/mmm* (No.191)
Lattices	$a = b = 5.5056(3)$ Å, $c = 8.9869(7)$ Å	$a = b = 5.5273(2)$ Å, $c = 9.0118(6)$ Å
	$V = 235.91(3)$ Å^3, $Z = 1$	$V = 238.43(2)$ Å^3, $Z = 1$
Absorption coefficient	31.070 mm^{-1}	30.741 mm^{-1}
F(000)	516.0	516.0
R_{int}	0.022	0.026
Reflections collected	5081	4016
Independent reflections	233	235
Extinction coefficient	0.0199(15)	0.061(4)
Data/restraints/parameters	233/1/20	235/1/20
Goodness-of-fit on F^2	1.316	1.362
Refine_diff_density_max	1.567	2.636
Refine_diff_density_min	−2.083	−3.533
R_1, $wR_2[I > 2\sigma]$	0.0192, 0.0529	0.0307,0.0686
R_1, wR_2(all data)	0.0192, 0.0529	0.0307,0.0686

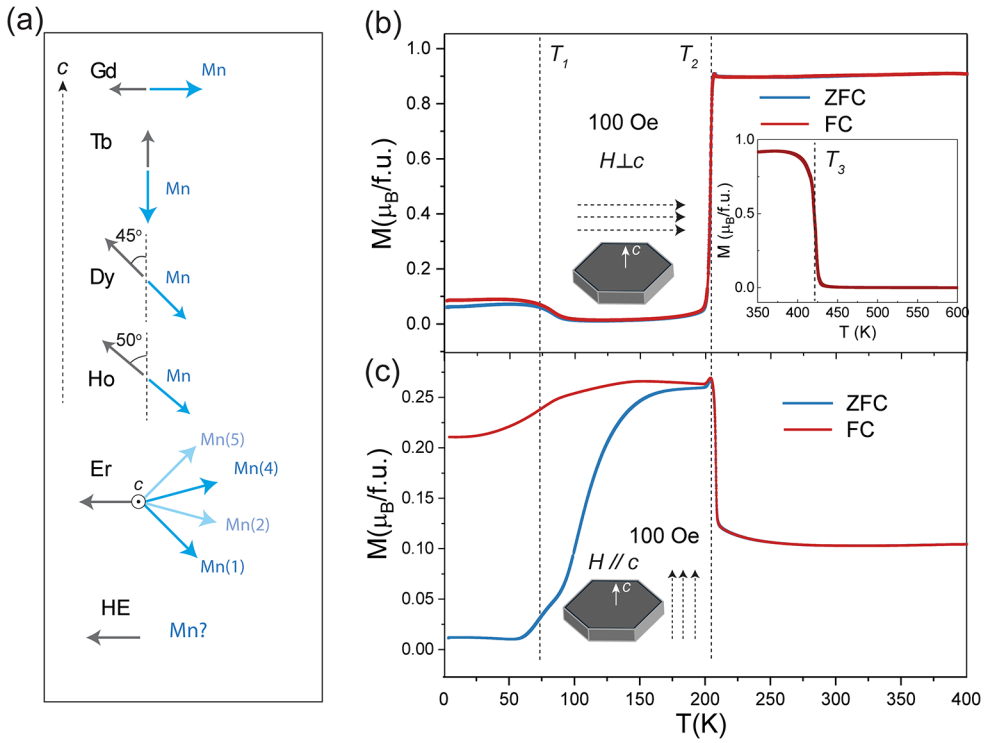

Figure 2. (a) Magnetic order of the parent phase with different rare-earth elements. (b, c) Temperature dependence of magnetization on HE166 with an external magnetic field applied perpendicular to and along the *c* axis. ZFC: zero field cooling. FC: field cooling. The inset shows the magnetization of HE166 in the FC mode in high-temperature regions of 350−600 K, which overlaps with the ZFC result and highlights the transition at T_3.

constructed using a set of 2404 measured ω scan frames for 123 K and 2097 for 300 K. The sharp Bragg peaks, free from heavy distortions like ring shapes or blurry spots, shows the high crystallinity in our single crystals, which is further confirmed by the good refinement results showing in the Table 1. X-ray diffraction and related refinements indicate that the HE166 crystal with five rare-earth elements has the same crystal structure as the parent phases, where the rare-earth elements are randomly distributed on the Wyckoff position 1a site. Moreover, we do not observe a structure change between 123 and 300 K within the resolution of the X-ray diffraction equipment, as shown in Figure 1a and Table 1, excluding a structure change at the magnetic phase transitions, which we will discuss later. The homogeneous distribution of the five rare-earth elements is further confirmed with energy-dispersive X-ray spectroscopy (Figure 1c). The measured composition of HE-166 from SEM-EDX is $(Gd_{0.21}Tb_{0.22}Dy_{0.22}Ho_{0.19}Er_{0.16})Mn_6Sn_6$, which is rather close but slightly different from the nominal evenly distributed (20% for each rare-earth) nominal composition starting the synthesis. The configurational entropy associated with the multicomponent rare-earth sublattice can be estimated as $S_{conf} = -R\sum_i x_i \ln x_i$, where x_i denotes the atomic fraction of each rare-earth element. For five equiatomic species (Gd, Tb, Dy, Ho, Er), configurational

https://doi.org/10.1021/acs.inorgchem.5c03461
Inorg. Chem. 2026, 65, 71−78

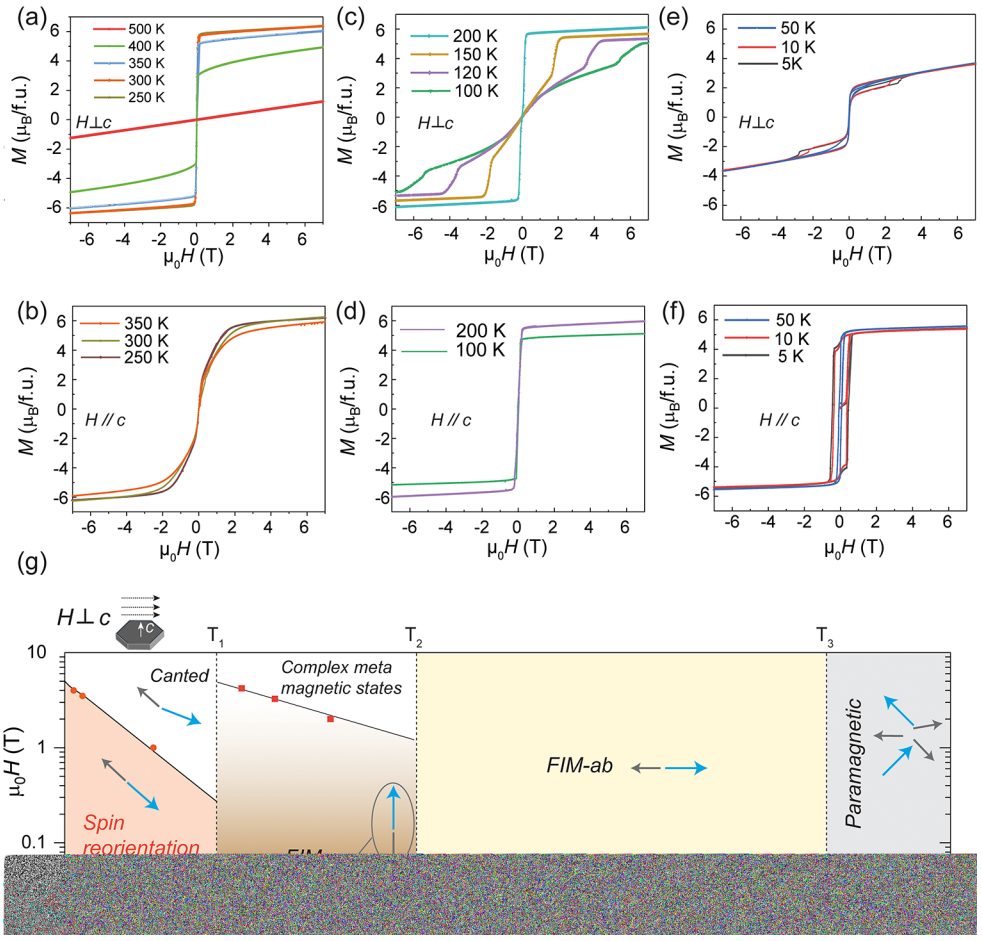

Figure 3. Field-dependent magnetization hysteresis loops of HE166 at various temperatures. (a), (c), (e) Measurements from 5−350 K with an external magnetic applied along the in-plane direction (H⊥c). (b), (d), (f) Measurements from 5−500 K with field applied along out-of-plane direction (H//c). (g) Magnetic phase diagram of HE166 with an external magnetic field applied perpendicular to the crystalline *c* direction. *FIM-ab*: in-plane ferrimagnetism. *FIM-c*: uniaxial ferrimagnetism. Light blue and gray arrows: magnetic orders of high-entropy rare-earth elements and Mn atoms, respectively.

entropy reaches 1.61R, exceeding the typical 1.5 R criterion for high-entropy phases.[21] It is interesting to note that HE-166 crystals are directly grown from elements without obvious other phase formation during the synthesis, while during single-rare-earth 166 phase synthesis, minor impurities such as RSn_2 with different crystal morphology is observed

The 166 parent phases exhibit different magnetic structures depending on the rare-earth element,[5,10,12,22−24] which is illustrated in Figure 2a. The light blue and gray arrows indicate the magnetic orders of Mn and rare-earth elements, respectively. In the high-entropy 166 system, where all the rare-earth elements occupy the same crystallographic site, no evidence of phase separation was observed in our single-crystal diffraction, chemical analysis, as well as magnetization measurements. Furthermore, the magnetic phases in the high-entropy 166 do not appear to be a superposition of parent phases containing only one rare-earth element. Instead, the competition among the different magnetic ions from Gd to Er leads to a richer magnetic phase diagram, including new transitions as well as new transition temperatures that do not appear in the parent phases. Figure 2b,c shows the temperature-dependent magnetizations of HE166 with the magnetic field applied along the in-plane and out-of-plane directions, respectively. Multiple magnetic transitions have been observed, which are marked as T_1, T_2, and T_3. Figure 2b shows the temperature dependence of magnetization when an external magnetic field is applied within the basal plane. Upon cooling from 600 K, a sudden increase in the magnetization occurs at 420 K, marked as T_3, indicating the paramagnetic to ferrimagnetic phase transition, as shown in the inset of Figure 2b. As the temperature continues to decrease to 200 K, the magnetization remains nearly constant, indicating the presence of a saturated in-plane ferrimagnetic order. Below 200 K, the magnetization drops dramatically, indicating that a spin reorientation occurs, where the in-plane ferrimagnetism changes to out-of-plane uniaxial ferrimagnetism, which we will discuss further later. Below 80 K, a slight splitting occurs between the zero-field cooling (ZFC) and field cooling (FC) magnetization, and this is related to another magnetic transition associated with the spin reorientation, as seen in other R166 systems.[19,25] Figure 2c shows the magnetization data when the external magnetic field is applied out-of-plane. A peak occurs at 200 K, corresponding to the spin reorientation. Slightly below 200 K, a splitting between ZFC and FC magnetization occurs. When the temperature continuously decreases, a small hump feature as well as kink-like behavior happen below 80 K, consistent with the in-plane measurements, jointly revealing the spin-reorientation transition. It should be noted that the ZFC and FC magnetization curves exhibit bifurcation at distinct temperatures depending on the

https://doi.org/10.1021/acs.inorgchem.5c03461
Inorg. Chem. 2026, 65, 71−78

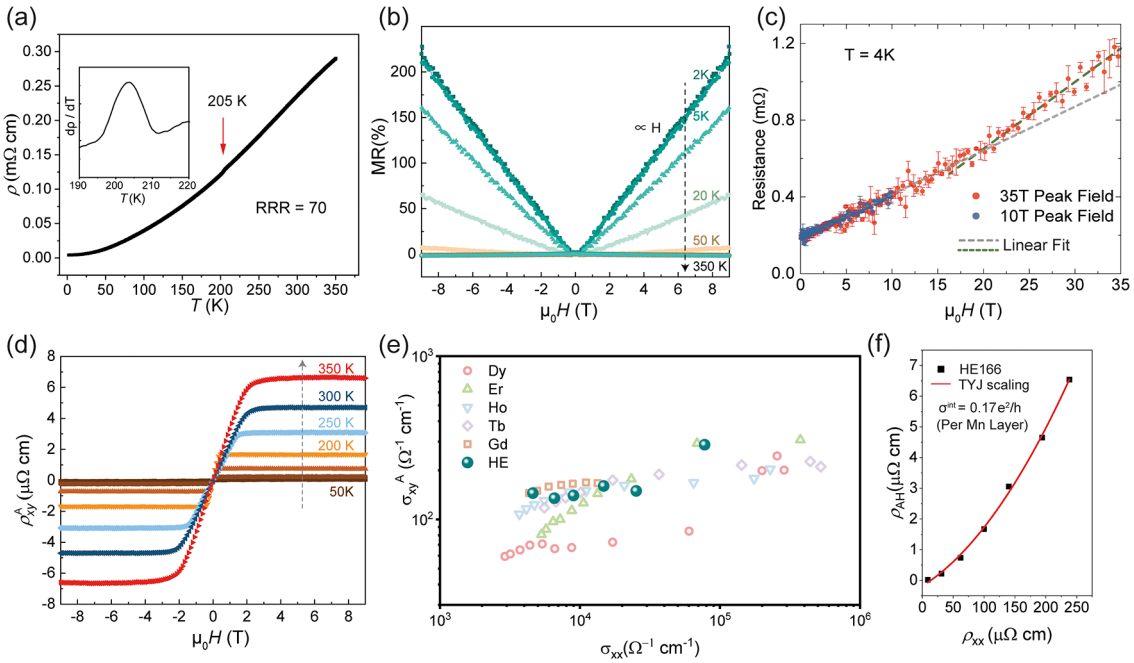

Figure 4. Electrical transport results for HE166. (a) Temperature-dependent resistivity of the HE166 system. (b) Magnetoresistance of HE166 from 0−9 T at various temperatures from 4−350 K. (c) Magnetoresistance of HE166 at 4 K in pulsed magnetic fields up to 35 T. (d) Hall resistivity of HE166 as a function of magnetic field at various temperatures. (e) Anomalous Hall conductivity vs longitudinal conductivity of HE166 (solid balls) and the parent phases (open circles). (f) Tian-Ye-Jin scaling of HE166.

field orientation. For $H\perp c$, the ZFC and FC curves start to diverge at T_1, while for $H\|c$, the bifurcation occurs at T_2. This behavior indicates strong magnetic anisotropy associated with coupling between the Mn−Kagome planes and the rare-earth layers. Moreover, the temperature dependence of C_p (Figure S2) shows a clear anomaly near 205 K, which coincides well with the magnetic transition temperature T_2. In contrast, the transition at T_1 is not detected in the specific heat measurements, most likely due to the very limited entropy change associated with the spin reorientation around T_1

To further understand the magnetic interactions, magnetic hysteresis loops at fixed temperatures were measured, as shown in Figure 3. These measurements reveal large anisotropies and rich magnetic behaviors in the HE166 system. When the external magnetic field is applied in-plane (H⊥c), the $M-H$ curve at 500 K shows a linear response, confirming paramagnetic behavior of HE166, as shown in Figure 3a. Upon cooling to 400 K, the magnetization undergoes a sharp increase and can reach saturation easily under a small external field. This saturation becomes more pronounced with further cooling. Similar magnetization behavior of HE166 is observed in the temperature range of 200−100 K when the magnetic field is applied out-of-plane (H//c), as shown in Figure 3e. They jointly indicate a reorientation of the ferrimagnetic easy axis from the in-plane to out-of-plane direction at 210 K, as revealed in the M (T) measurement in Figure 2.

The field-induced magnetization exhibits dramatically different behavior when the external field is applied perpendicular to the easy axis of ferrimagnetic order at different temperatures, as shown in Figure 3b,c. In Figure 3b (H//c), the magnetization between 350 and 250 K increases gradually before reaching saturation, indicating a continuous spin reorientation as the ferrimagnetic order is forced to align with the external field. In contrast, Figure 3c (H⊥c) shows that metastable magnetic states are easily induced between 200 and 100 K when the external magnetic field is perpendicular to the ferrimagnetic order. For example, at 150 K, the magnetization increases gradually until a sharp jump at 2 T, followed by a slow increase toward saturation above 3 T. Such an unusual magnetization resembles the topological Hall effect, which has been revealed in $ErMn_6Sn_6$.[10]

Below 50 K, both the magnetization curves with H//c and H⊥c share common features of hysteresis loops, which become more prominent upon cooling, as seen in Figure 3e,f. The formation of hysteresis loops indicates the deviation of the easy axis of FIM order from the c axis, as shown in the Dy, Ho, and Er 166 parent systems.[13,22] It should be noted that the magnetization does not saturate with H⊥c, as seen in Figure 3e, suggesting the formation of spin canting, where the magnetic moments of the Mn and rare-earth elements tilt away from a collinear alignment.

Considering all of the magnetization results, a magnetic phase diagram is constructed with the external magnetic field applied perpendicular to the crystalline c direction ($H\perp c$), as shown in Figure 3g. The competition between the multiple factors like exchange, anisotropy, and Zeeman energies[10] yields a rich magnetic phase diagram. Above T_3, thermal spin fluctuations dominate, and the whole system shows paramagnetic behavior. Below T_3 and above T_2, the exchange energy prevails, stabilizing a long-range planar ferrimagnetic order. When the temperature further decreases below T_2 but above T_1, this ferrimagnetic order reorients from the in-plane direction to the out-of-plane direction due to the dominance of the out-of-plane anisotropy energy. Notably, within this intermediate temperature range from 80 to 200 K, the out-of-plane magnetic state exhibits complex metamagnetic behavior under in-plane magnetic fields, with $M-H$ loops suggestive of nonzero scalar spin chirality and potentially chiral spin textures.[7−9,26] Verification of such states requires advanced neutron diffraction studies. Below T_1, thermal

https://doi.org/10.1021/acs.inorgchem.5c03461
Inorg. Chem. 2026, 65, 71−78

fluctuations are further suppressed, and the anisotropy energy increasingly governs the spin configuration, inducing an additional spin reorientation in which the FIM easy axis tilts away from the *c* axis toward an intermediate direction between the *c* axis and the *ab* plane. Under external magnetic fields, the Mn and rare-earth moments develop slightcanting, forming canted spin textures.

Besides magnetization measurements, electrical transport measurements were also carried out to understand the band topology in the high-entropy Kagome lattice HE166. In-plane resistivity as a function of temperature and magnetic field is shown in Figure 4. The ρ(T) indicates the metallic nature of the sample over the whole temperature range 2−350 K, which is similar to the parent phases. The residual resistance ratio (RRR) defined as RRR = R_{xx}(300 K)/R_{xx} (2 K), is about 70, indicating the high quality of our crystals despite the additional electron scattering caused by high-entropy alloying. The derivative of resistivity shows a small yet clear peak at 205 K, as shown in Figure 4a inset, which is correlated with the magnetic transition T_2 discussed previously. Magnetoresistance $MR = [\rho_{xx}(H)-\rho_{xx}(0)]/\rho_{xx}(0) \times 100\%$ is shown on Figure 4b. A clear nonsaturating linear MR with a ratio of 225% at 2 K is observed. Compared to the parent phases, HE166 with five rare-earth elements shows enhanced linear behavior, which may arise from the high entropy.[23] As the temperature increases, the MR keeps its linearity with a reduced MRR ratio.

To explore further the extent of the linear MR in HE166, the MR was measured at T = 4 K under higher magnetic fields in a pulsed magnet with peak fields of 10 and 35 T, as shown in Figure 4c. The linearity remains until the magnetic field reaches 20 T, where a kink occurs and is followed by another relatively linear MR regime. There are no signs of saturation for the second linear MR behavior up to 35 T. The kink around 20 T has never been reported in the parent phases of Gd, Tb, Dy, and Ho166 systems. In the case of $ErMn_6Sn_6$, which is close to the boundary of spiral magnetism and ferrimagnetism, several theoretical works report FIM to canned magnetic structures occur for all the parent phases around 20 T.[10,27] The change in the coupling between Er and Mn around 20 T seems a plausible reason for the kink in the HE166 system here.

Furthermore, the anomalous Hall effect can reveal subtle interactions between localized moments and itinerant electrons that cannot be captured by conventional transport measurements. The evolution of anomalous Hall resistivity with temperature can help distinguish contributions from intrinsic mechanisms and the extrinsic scattering process. The former is generally related to band topology, and the latter is involved with the impurity-induced side jump and skew scattering.[28−31] The anomalous Hall resistivity is separated via the empirical relation,

$$\rho_{xy} = \rho_{xy}^{0} + \rho_{xy}^{A} = R_0 B + 4\pi R_s M$$

Here, the first term ρ_{xy}^{0} indicates the normal Hall resistivity, and the second term represents the anomalous Hall effect, which is correlated with the magnetic order in the system. We focus on the second term. When the temperature increases, the saturation value of ρ_{xy} becomes bigger. However, in the low temperature region below 50 K, the noise is too large due to the small signal, which we will not take into consideration. The conductivity tensors of σ_{xx} and σ_{xy} are derived by $\sigma_{xx} = \rho_{xx}/(\rho_{xy}^2 + \rho_{xx}^2)$ and $\sigma_{xy} = \rho_{xy}/(\rho_{xy}^2 + \rho_{xx}^2)$. The scaling behavior between σ_{xy} and σ_{xx} of HE166 and the parent phases is shown in Figure 4e. HE166 shows trends similar to those of the parent phases. All the σ_{xy} are weakly linked to σ_{xx} and clearly deviate from a linear relation, a characteristic of an extrinsic mechanism like screw scattering and side jump, instead of an origin from disorder or impurities.[28] The deviations of the linear relation indicate the contributions from the intrinsic term, which depends only on the band structure and indicates the existence of nontrivial band structures such as Berry curvatures. To extract the intrinsic Hall conductivity, the Tian-Ye-Jin scaling law is utilized.[32]

$$\rho_{xy}^{A} = \sigma_{\text{int}}\rho_{xx}^{2} + \sigma_{\text{skew}}\rho_{xx}$$

σ_{int} is estimated to be 66 $\Omega^{-1}\text{cm}^{-1}$. For each Mn layer, the σ_{int} is estimated to be 0.17 e^2/h. The parent phases show σ_{int} ranges from 0.04−0.27 e^2/h per Mn Layer.[6,13,23,33] As a result, the estimated σ_{int} in the high-entropy phase is close to the average value of the parent phases,[13] providing another piece of evidence for the modulation of the topological phases in the R166 system through high-entropy engineering.

4. CONCLUSIONS

In summary, we have synthesized a high-configurational entropy kagome lattice with the five rare-earth elements of Gd, Tb, Dy, Ho, and Er. The homogeneous distribution of disorder among the rare-earth elements can be stabilized by high configurational entropy. These homogeneous disorders lead to variations in exchange coupling that compete with magnetic anisotropy and Zeeman energies, thereby inducing the observed changes in magnetic and transport phenomena, including multiple temperature- and field-induced transitions, ultralinear magnetoresistance persisting up to 20 T at 4 K, etc. Furthermore, such disorders give rise to local lattice distortions, exchange-field fluctuations, and site-dependent crystal electric fields due to differences in ionic radii, 4f moment sizes, and spin−orbit coupling strengths. Collectively, these intrinsic fluctuations modify long-range magnetic coherence and introduce competing exchange pathways. It should be noted that in many high-entropy materials, including our 166 HE phases, numerous emergent properties cannot be directly attributed to individual components; instead, they are generally ascribed to the so-called "cocktail effect",[21] the precise mechanisms of which remain an open question. Our study of the HE166 system, combined with the previously reported high-entropy phases with four rare-earth elements,[19] offer a glimpse into a vast compositional landscape that holds high promises for uncovering new magnetic and topological phenomena.

■ ASSOCIATED CONTENT

Supporting Information

The Supporting Information is available free of charge at https://pubs.acs.org/doi/10.1021/acs.inorgchem.5c03461.

Magnetization for HE166 with varying number of rare-earth elements and specific heat result of (Gd,Tb,Dy,Ho,Er)Mn_6Sn_6 (PDF)

Accession Codes

Deposition Numbers 2513131−2513132 contain the supplementary crystallographic data for this paper. These data can be obtained free of charge via the joint Cambridge Crystallo-

https://doi.org/10.1021/acs.inorgchem.5c03461
Inorg. Chem. 2026, 65, 71−78

graphic Data Centre (CCDC) and Fachinformationszentrum Karlsruhe Access Structures service.

AUTHOR INFORMATION

Corresponding Author

Bing Lv − *Department of Physics, the University of Texas at Dallas, Richardson, Texas 75080, United States;* orcid.org/0000-0002-9491-5177; Email: blv@utdallas.edu

Authors

Wenhao Liu − *Department of Physics, the University of Texas at Dallas, Richardson, Texas 75080, United States; Department of Physics, University of California, Berkeley, California 94720, United States; Material Sciences Division, Lawrence Berkeley National Lab, Berkeley, California 94720, United States;* orcid.org/0000-0001-9757-1077

Nikhil Uday Dhale − *Department of Physics, the University of Texas at Dallas, Richardson, Texas 75080, United States*

Youzhe Chen − *Department of Physics, University of California, Berkeley, California 94720, United States; Material Sciences Division, Lawrence Berkeley National Lab, Berkeley, California 94720, United States*

Pramanand Joshi − *Department of Physics, the University of Texas at Arlington, Arlington, Texas 76019, United States;* orcid.org/0000-0003-2245-6618

Zixin Zhai − *Department of Physics, the University of Texas at Dallas, Richardson, Texas 75080, United States*

Xiqu Wang − *Department of Chemistry, University of Houston, Houston, Texas 77204, United States*

J. Ping Liu − *Department of Physics, the University of Texas at Arlington, Arlington, Texas 76019, United States;* orcid.org/0000-0001-7978-6357

Robert J. Birgeneau − *Department of Physics, University of California, Berkeley, California 94720, United States; Material Sciences Division, Lawrence Berkeley National Lab, Berkeley, California 94720, United States*

Boris Maiorov − *National High Magnetic Field Laboratory, Los Alamos National Laboratory, Los Alamos, New Mexico 87545, United States*

Christopher A. Mizzi − *National High Magnetic Field Laboratory, Los Alamos National Laboratory, Los Alamos, New Mexico 87545, United States*

Complete contact information is available at: https://pubs.acs.org/10.1021/acs.inorgchem.5c03461

Notes

A preprint of this manuscript has been posted on arxiv[34] prior to the final publication.

The authors declare no competing financial interest.

ACKNOWLEDGMENTS

The work conducted at the University of Texas at Dallas was supported by the US Air Force Office of Scientific Research Grant No. FA9550-19-1-0037, National Science Foundation-DMREF-2324033, and Office of Naval Research grant no. N00014-23-1-2020. A portion of this work was performed at the National High Magnetic Field Laboratory, which is supported by the National Science Foundation Cooperative Agreement No. DMR-2128556, the State of Florida, and the Department of Energy. Work at the University of California, Berkeley, and Lawrence Berkeley National Laboratory was funded by the U.S. DOE, Office of Science, Office of Basic Energy Sciences, Materials Sciences and Engineering Division under Contract No. DE-AC02-05CH11231 (Quantum Materials Program KC2202).

REFERENCES

(1) Ying, T.; Yu, T.; Shiah, Y.-S.; Li, C.; Li, J.; Qi, Y.; Hosono, H. High-Entropy van Der Waals Materials Formed from Mixed Metal Dichalcogenides, Halides, and Phosphorus Trisulfides. *J. Am. Chem. Soc.* **2021**, *143* (18), 7042−7049.

(2) Jiang, K.; Wu, T.; Yin, J.-X.; Wang, Z.; Hasan, M. Z.; Wilson, S. D.; Chen, X.; Hu, J. Kagome Superconductors AV3Sb5 (A = K, Rb, Cs). *Natl. Sci. Rev.* **2023**, *10* (2), No. nwac199.

(3) Bernevig, B. A.; Felser, C.; Beidenkopf, H. Progress and Prospects in Magnetic Topological Materials. *Nature* **2022**, *603* (7899), 41−51.

(4) Mazin, I. I.; Jeschke, H. O.; Lechermann, F.; Lee, H.; Fink, M.; Thomale, R.; Valentí, R. Theoretical Prediction of a Strongly Correlated Dirac Metal. *Nat. Commun.* **2014**, *5* (1), No. 4261.

(5) Malaman, B.; Venturini, G.; Welter, R.; Sanchez, J. P.; Vulliet, P.; Ressouche, E. Magnetic Properties of RMn6Sn6 (R = Gd−Er) Compounds from Neutron Diffraction and Mössbauer Measurements. *J. Magn. Magn. Mater.* **1999**, *202* (2−3), 519−534.

(6) Yin, J.-X.; Ma, W.; Cochran, T. A.; Xu, X.; Zhang, S. S.; Tien, H.-J.; Shumiya, N.; Cheng, G.; Jiang, K.; Lian, B.; Song, Z.; Chang, G.; Belopolski, I.; Multer, D.; Litskevich, M.; Cheng, Z.-J.; Yang, X. P.; Swidler, B.; Zhou, H.; Lin, H.; Neupert, T.; Wang, Z.; Yao, N.; Chang, T.-R.; Jia, S.; Hasan, M. Z. Quantum-Limit Chern Topological Magnetism in TbMn6Sn6. *Nature* **2020**, *583* (7817), 533−536.

(7) Ghimire, N. J.; Dally, R. L.; Poudel, L.; Jones, D. C.; Michel, D.; Magar, N. T.; Bleuel, M.; McGuire, M. A.; Jiang, J. S.; Mitchell, J. F.; Lynn, J. W.; Mazin, I. I. Competing Magnetic Phases and Fluctuation-Driven Scalar Spin Chirality in the Kagome Metal YMn6Sn6. *Sci. Adv.* **2020**, *6* (51), No. eabe2680.

(8) Zhang, H.; Liu, C.; Zhang, Y.; Hou, Z.; Fu, X.; Zhang, X.; Gao, X.; Liu, J. Magnetic Field-Induced Nontrivial Spin Chirality and Large Topological Hall Effect in Kagome Magnet ScMn6Sn6. *Appl. Phys. Lett.* **2022**, *121* (20), No. 202401.

(9) Madhogaria, R. P.; Mozaffari, S.; Zhang, H.; Meier, W. R.; Do, S.-H.; Xue, R.; Matsuoka, T.; Mandrus, D. G. Topological Nernst and Topological Thermal Hall Effect in Rare-Earth Kagome ScMn6Sn6. *Phys. Rev. B* **2023**, *108* (12), No. 125114.

(10) Riberolles, S. X. M.; Han, T.; Slade, T. J.; Wilde, J. M.; Sapkota, A.; Tian, W.; Zhang, Q.; Abernathy, D. L.; Sanjeewa, L. D.; Bud'ko, S. L.; Canfield, P. C.; McQueeney, R. J.; Ueland, B. G. New Insight into Tuning Magnetic Phases of RMn6Sn6 Kagome Metals. *npj Quantum Mater.* **2024**, *9* (1), No. 42.

(11) Samatham, S. S.; Casey, J.; Szucs, A. M.; Yenugonda, V.; Burgio, C.; Siegrist, T.; Pathak, A. K. Perturbation-Tuned Triple Spiral Metamagnetism and Tricritical Point in Kagome Metal ErMn6Sn6. *Commun. Mater.* **2024**, *5* (1), No. 113.

(12) Fruhling, K.; Streeter, A.; Mardanya, S.; Wang, X.; Baral, P.; Zaharko, O.; Mazin, I. I.; Chowdhury, S.; Ratcliff, W. D.; Tafti, F. Topological Hall Effect Induced by Chiral Fluctuations in ErMn6Sn6. *Phys. Rev. Mater.* **2024**, *8* (9), No. 094411.

(13) Ma, W.; Xu, X.; Yin, J.-X.; Yang, H.; Zhou, H.; Cheng, Z.-J.; Huang, Y.; Qu, Z.; Wang, F.; Hasan, M. Z.; Jia, S. Rare Earth Engineering in RMn6Sn6 (R = Gd-Tm, Lu) Topological Kagome Magnets. *Phys. Rev. Lett.* **2021**, *126* (24), No. 246602.

(14) Ying, T.; Yu, T.; Qi, Y.; Chen, X.; Hosono, H. High Entropy van Der Waals Materials. *Adv. Sci.* **2022**, *9* (30), No. 2203219.

(15) George, E. P.; Raabe, D.; Ritchie, R. O. High-Entropy Alloys. *Nat. Rev. Mater.* **2019**, *4* (8), 515−534.

(16) Toher, C.; Oses, C.; Esters, M.; Hicks, D.; Kotsonis, G. N.; Rost, C. M.; Brenner, D. W.; Maria, J.-P.; Curtarolo, S. High-Entropy Ceramics: Propelling Applications through Disorder. *MRS Bull.* **2022**, *47* (2), 194−202.

(17) Kotsonis, G. N.; Almishal, S. S. I.; Vieira, F. M.; dos, S.; Crespi, V. H.; Dabo, I.; Rost, C. M.; Maria, J. High-entropy Oxides:

Harnessing Crystalline Disorder for Emergent Functionality. *J. Am. Ceram. Soc.* **2023**, *106* (10), 5587−5611.
(18) Chatterjee, A.; Ganguly, D.; Sundara, R.; Bhattacharya, S. S. High-Entropy Cubic Perovskite Oxide-Based Solid Electrolyte in Quasi-Solid-State Li−S Battery. *Energy Technol.* **2024**, *12* (1), No. 2300576, DOI: 10.1002/ente.202300576.
(19) Min, L.; Sretenovic, M.; Heitmann, T. W.; Valentine, T. W.; Zu, R.; Gopalan, V.; Rost, C. M.; Ke, X.; Mao, Z. A Topological Kagome Magnet in High Entropy Form. *Commun. Phys.* **2022**, *5* (1), No. 63.
(20) Leroux, M.; Balakirev, F. F.; Miura, M.; Agatsuma, K.; Civale, L.; Maiorov, B. Dynamics and Critical Currents in Fast Superconducting Vortices at High Pulsed Magnetic Fields. *Phys. Rev. Appl.* **2019**, *11* (5), No. 054005.
(21) Sen, S.; Palabathuni, M.; Ryan, K. M.; Singh, S. High Entropy Oxides: Mapping the Landscape from Fundamentals to Future Vistas. *ACS Energy Lett.* **2024**, *9* (8), 3694−3718.
(22) Jones, D. C.; Das, S.; Bhandari, H.; Liu, X.; Siegfried, P.; Ghimire, M. P.; Tsirkin, S. S.; Mazin, I. I.; Ghimire, N. J. Origin of Spin Reorientation and Intrinsic Anomalous Hall Effect in the Kagome Ferrimagnet TbMn6Sn6. *Phys. Rev. B* **2024**, *110* (11), No. 115134.
(23) Gao, L.; Shen, S.; Wang, Q.; Shi, W.; Zhao, Y.; Li, C.; Cao, W.; Pei, C.; Ge, J.-Y.; Li, G.; Li, J.; Chen, Y.; Yan, S.; Qi, Y. Anomalous Hall Effect in Ferrimagnetic Metal RMn6Sn6 (R = Tb, Dy, Ho) with Clean Mn Kagome Lattice. *Appl. Phys. Lett.* **2021**, *119* (9), No. 092405.
(24) Zeng, H.; Yu, G.; Luo, X.; Chen, C.; Fang, C.; Ma, S.; Mo, Z.; Shen, J.; Yuan, M.; Zhong, Z. Large Anomalous Hall Effect in Kagomé Ferrimagnetic HoMn6Sn6 Single Crystal. *J. Alloys Compd.* **2022**, *899*, No. 163356.
(25) Wang, Z.; Xu, J.; Li, Z.; Xu, T.; Li, J.; Zhao, T.; Cai, J.; Zhang, Y.; Shen, B. Real-Space Observation of Magnetic Transitions in RMn6Sn6 (R = Ho, Dy) Kagome Magnets. *Appl. Phys. Lett.* **2023**, *122* (11), No. 112401.
(26) Wang, Q.; Neubauer, K. J.; Duan, C.; Yin, Q.; Fujitsu, S.; Hosono, H.; Ye, F.; Zhang, R.; Chi, S.; Krycka, K.; Lei, H.; Dai, P. Field-Induced Topological Hall Effect and Double-Fan Spin Structure with a c-Axis Component in the Metallic Kagome Antiferromagnetic Compound YMn6Sn6. *Phys. Rev. B* **2021**, *103* (1), No. 014416.
(27) L, N.; Trevisan, T. V.; McQueeney, R. J. High-Field Magnetic Phase Diagrams of the RMn6Sn6 (R = Gd−Tm) Kagome Metals. *Phys. Rev. B* **2025**, *111* (5), No. 054410.
(28) Nagaosa, N.; Sinova, J.; Onoda, S.; MacDonald, A. H.; Ong, N. P. Anomalous Hall Effect. *Rev. Mod. Phys.* **2010**, *82* (2), 1539−1592.
(29) Yang, S. A.; Pan, H.; Yao, Y.; Niu, Q. Scattering Universality Classes of Side Jump in the Anomalous Hall Effect. *Phys. Rev. B* **2011**, *83* (12), No. 125122.
(30) Berger, L. Side-Jump Mechanism for the Hall Effect of Ferromagnets. *Phys. Rev. B* **1970**, *2* (11), 4559−4566.
(31) Karplus, R.; Luttinger, J. M. Hall Effect in Ferromagnetics. *Phys. Rev.* **1954**, *95* (5), 1154−1160.
(32) Tian, Y.; Ye, L.; Jin, X. Proper Scaling of the Anomalous Hall Effect. *Phys. Rev. Lett.* **2009**, *103* (8), No. 087206.
(33) Asaba, T.; Thomas, S. M.; Curtis, M.; Thompson, J. D.; Bauer, E. D.; Ronning, F. Anomalous Hall Effect in the Kagome Ferrimagnet GdMn6Sn6. *Phys. Rev. B* **2020**, *101* (17), No. 174415.
(34) Liu, W.; Dhale, N. U.; Chen, Y.; Joshi, P.; Zhai, Z.; Wang, X.; Liu, P.; Birgeneau, R. J.; Maiorov, B.; Mizzi, C. A.; Lv, B. High Entropy Engineering of Magnetic Kagome Lattice (Gd,Tb,Dy,Ho,Er)-Mn_6Sn_6. 2025 arXiv:2507.22809. arXiv.org e-Printarchive. https://arxiv.org/abs/2507.22809 DOI: 10.48550/arXiv.2507.22809.